

# Multi-Harmonic Gridded 3D Deconvolution (MH3D) for Robust and Accurate Image Reconstruction in MPI for Single Axis Drive Field Scanners

Toby Sanders, Justin J. Konkle, Erica E. Mason, Patrick W. Goodwill

## Abstract

This article presents a new robust model for image reconstruction in magnetic particle imaging (MPI) for single-axis drive field scans, which is based on the deconvolution of gridded harmonic data. Gridded harmonic data, used commonly in MPI, does not map to underlying iron density but rather to the iron density convolved with the harmonic point-spread functions. We refer to the gridded harmonic data as *harmonic portraits*, since they only represent a portrait-like representation of the iron density, and a deconvolution method is implemented to reconstruct the true underlying density. The advantage of this new method is primarily in the intermediate data analysis that comes in the harmonic portrait domain, where we are able to perform artifact correction, parameter selection, and general data assessment and calibrations efficiently. Furthermore, we show with several examples that our new method closely compares qualitatively with current state-of-the-art image reconstruction models in MPI. While the general concept of gridding harmonic data in MPI is not new, the complete modeling and characterization in order to use the data for image reconstruction has remained an ongoing area of research. We provide detailed analysis, theoretical insights, and many nuanced techniques that make our new methodology and algorithm accurate and robust.

## 1 Introduction

Magnetic particle imaging (MPI) is an emerging medical imaging modality that can map superparamagnetic iron oxide nanoparticle (SPION) concentrations in the human body. It offers a unique set of imaging capabilities complimentary to traditional imaging modalities like MRI, CT scans, and ultrasound, and can produce linear, quantifiable, high-resolution images of the SPION tracers [2, 3, 10, 18, 21]. The potential medical applications of MPI are currently a very active area of research and include but are not limited to cardiovascular (perfusion) imaging, cell tracking, and sentinel lymph node imaging [18, 22–25, 27]. The list of applications will continue to evolve and expand as the MPI technology transitions from the preclinical research space and into clinical labs and hospitals.

The work in this article focuses on a fundamental component of MPI, the image reconstruction problem, the process by which the raw signal data acquired from the scan is processed to form images representing the SPION maps. Our new method develops a complete model utilizing the full breadth of information in the MPI signal and is based on deconvolution of *harmonic portrait* data. The advantage of this new model is in the intermediate harmonic portrait domain, where we can easily analyze the data, correct potential artifacts, and tune and select parameters based on the data analysis.

An MPI scanner works by selectively exciting magnetic particles with an oscillating drive field. Receive coils then detect the change in magnetization of the particles induced by the drive field. The received time domain signal data is then used to reconstruct the SPION density map. The unique property of the SPIONs is that their magnetization response to the magnetic field is given by the nonlinear Langevin function, which allows for harmonic signals necessary for MPI.

The static gradient magnetic field,  $H(\vec{x})$ , creates a field free region (FFR), which is either a field free point (FFP) or field free line (FFL) in 3D. The drive field causes the FFR to oscillate and the particles near the FFR to selectively experience a change in magnetization, while the particles far from the FFR remain in a saturated magnetic state as characterized by the Langevin function. This effect creates spatially localized

information about the SPION density in the received signal, which allows for accurate image reconstruction when paired with FFR location information.

## 1.1 Contribution

This work develops a new model-based method for image reconstruction in MPI, which is rooted in characterizing the signals at its harmonics. The harmonics are located at integer multiple frequencies of the drive frequency,  $k \cdot f_0$ , where  $f_0$  is the sinusoidal drive field frequency and  $k$  is an integer greater than one<sup>1</sup>. Empirically, the signal spreads to a specific bandwidth around each harmonic defined by the shift field frequency, gradient, and particle characteristics.

We refer to our method as multi-harmonic 3D deconvolution (MH3D). The term *multi-harmonic* refers to the idea that we first compress the signal into a harmonic domain by interpolating the filtered harmonic data onto the FFP locations. This compressed data form we refer to as *harmonic portraits*, since they represent a portrait-like representation of the SPIONs, with unique *signatures* at each harmonic. These portraits are then used to compute a multi-frame 3D deconvolution to form the image reconstruction. Each of the portraits could in principle be used individually as a single-frame deconvolution, but using multiple harmonics together improves the resolution both theoretically and empirically.

Recently, a complete physics based computational image reconstruction model was developed for MPI [19], which was amendable to arbitrary scanning parameters and geometries. This current work is also a physics-based image reconstruction model, however it does not trivially generalize to arbitrary scanning parameters. It does however offer the distinct advantage of operating in the intermediate portrait domain, which allows for careful data analysis and complementary data processing prior to image reconstruction (see some of the methods outlined in Section 4). For example, we can detect and filter background signal, analyze which harmonics to use, select reconstruction parameters, and implement very simple data calibration methods that have so far been less trivial for the former generalized model. This portrait domain analysis also allows for detection and debugging of potential scanner hardware issues and allows for quick *intermediate* image visuals during a scan instead of waiting for the full reconstruction. For these reasons, MH3D has been an important tool for progress in our group’s work for both software and hardware development, while the former model will also continue to be an important tool in the future of MPI as the technology continues to progress.

Another important result of MH3D is the theoretical analysis of the mathematical components of MPI that fall out of the methodology. We present many known concepts in MPI from this new perspective, and also some lesser-known concepts, such as which harmonics are most important in MPI and how many are needed for image reconstruction. This work primarily focuses on the important algorithmic components of MH3D, while some of these theoretical components are also provided to support the methodology and understanding.

The concept for MH3D is applicable for a somewhat general set of scanner geometries. However, we primarily focus the mathematical descriptions from the viewpoint of our scanner’s hardware to keep the details concise and aligned. Section 2 outlines the scanner parameters, and most of the descriptions thereafter assume this particular set up. The major concepts behind MH3D are provided in Section 3. Additional but fundamental details behind MH3D are given in Section 4, while several examples are provided along the way to support the ideas presented.

## 1.2 Related Previous Approaches in MPI

While gridding/interpolating the harmonic data into a *portrait-like* domain is not a new concept within the MPI community, there have been a variety of different ideas about how to utilize this gridded data to form an accurate reconstructed image. The methodology laid out in this work provides a formal mathematical characterization and model for such data. Likewise, corresponding numerical methods and pragmatic calibration and tuning techniques are provided for robust image reconstruction.

A number of published works have utilized only the 3rd harmonic signal [9, 15–17]. In some cases, the images presented are the 3rd harmonic portraits, which only represent the object for the case of SPION

---

<sup>1</sup>The fundamental harmonic at  $f_0$  is absent in the MPI receive signal due to the necessary receive chain filter of the excitation drive field.

distributions limited to near the drive field’s DC bias location. However, this approach does not generalize for 3D objects without properly accounting for the 3D shape of the harmonic PSF. In the single-harmonic work of [9], the convolutional relationship between image and the harmonic PSF is correctly identified, and the 1D PSF shown in figure (5). However, this relationship is not directly utilized in the reconstruction, which is solved via a measured system matrix approach.

Other works have utilized multi-harmonic portraits, with varying approaches. For example, in the work of [12], the authors define in equation (9) of the article a very similar definition that we use for a *harmonic portrait* in our current work (defined later in this article in equation (5)). However, they do not utilize them in a technically accurate way, by instead only forming the final image by taking a weighted sum of the different harmonic images. The concepts laid out in this work will show that while such an approach may potentially provide some empirically suitable images for short term progress in MPI, it is not a technically sound methodology that should be applied in the longer term.

In the work of [14], the authors implemented a tomographic projection-based reconstruction from what can also be considered 2D projection *harmonic portraits*. This application was constrained to work for 2D acquisitions, based on temporal resolution requirements for their target application. Therefore the method they developed was used to inform the reconstruction of a 2D image, dealing with the inherently 3D SPION distributions.

Finally, there are two leading image reconstruction approaches in MPI that have received a great deal of attention. These are the system matrix (SM) approaches [10,11] and the X-space stitching approaches [6,7]. These approaches have been fundamental to the advancement of MPI field over the last decade. However, comparison with these methods is largely avoided in this text, since they are fundamentally different from the current work. Our current method most closely relates to the physics-based model discussed in the previous section [19], and the reader can refer to the discussion and results in that article for detailed comparisons with both X-space and SM. For more details about the state and history of image reconstruction in MPI, see [26].

## 2 FFP Scanning Geometry

Our scanner operates using an FFP with a static linear magnetic gradient field given by

$$H(\vec{x}) = G\vec{x} = G_0 \cdot \left[ \frac{x}{2}, \quad \frac{y}{2}, \quad z \right]^T, \quad (1)$$

where  $G_0 = 0.554$  T/m. The transmit drive coil excites along the  $z$ -axis, which defines the drive field given by

$$H_D(t) = [0, \quad 0, \quad B_{ex} \sin(2\pi f_0 t)]^T, \quad (2)$$

where  $B_{ex}$  is the excitation amplitude. The position excursion in meters of the FFR due to the drive field is  $A = B_{ex}/G$ . The slow shift fields, sometimes called the *focus field*, rasters in a zig-zag pattern in an  $xy$  plane for a fixed  $z$  location. We refer to this scan at a fixed  $z$  position as a  $z$ -slab. Figure 1 (c) demonstrates our FFP scanning trajectory for a single  $z$ -slab.

Multiple  $z$  positions are acquired to obtain a full 3D FFP data acquisition for image reconstruction. The  $z$ -slab positions are  $\{z_j\}_{j=1}^{N_z}$ , where  $N_z$  is the total number of slabs. The slabs are monotonically increasing,  $z_1 < z_2 < \dots < z_{N_z}$ , and equally spaced with  $\Delta z = z_{j+1} - z_j$ . Furthermore,  $\Delta z$  is chosen so that the FFP trajectories between neighboring slabs overlap, which can be expressed as  $\Delta z < 2A$ .

The received time domain MPI signal for a single  $z$ -slab is given in [5] by

$$s(t; z_j) = m \frac{d}{dt} \iiint \rho(\vec{x}) \vec{b}_1(\vec{x})^T \frac{H_j(\vec{x}, t)}{\|H_j(\vec{x}, t)\|} \mathcal{L}(\beta \|H_j(\vec{x}, t)\|) d\vec{x}, \quad (3)$$

where

- $\rho$  is the SPION density to image.
- $H_j(\vec{x}, t)$  is the total magnetic field for the scanned slab  $z_j$  at time  $t$ .
- $\mathcal{L}$  is the Langevin function given by  $\mathcal{L}(x) = \coth(x) - 1/x$ .

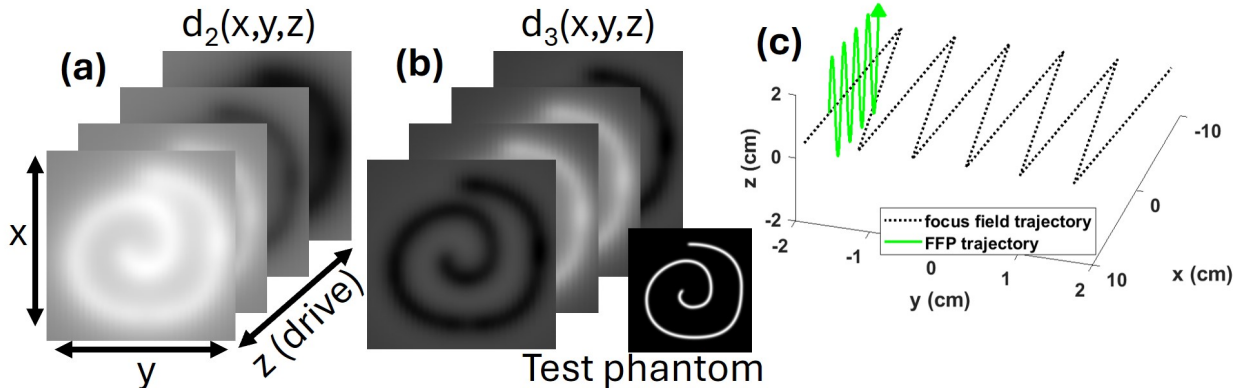


Figure 1: (a) and (b) show the 2nd and 3rd harmonic portraits at 4 consecutive  $z$ -slabs for a spiral phantom (shown in the bottom right of (b)) located in a plane at  $z = 0$ . (c) demonstrates the FFP scanning trajectory for a single  $z$ -slab.

- $\beta$  is a conglomerate SPION and scanner dependent constant, given by  $\beta = \frac{\mu_0 m}{\kappa_B T}$ , where  $T$  is temperature,  $m$  is the SPION specific magnetic moment,  $\kappa_B$  is the Boltzmann constant, and  $\mu_0$  is the vacuum permeability.
- $m$  is the SPION(s) magnetic moment.
- $\vec{b}_1$  is the vector field of spatially varying receive coil sensitivity values.

We denote the FFP location for each slab  $z_j$  at time  $t$  by  $\vec{\xi}_j(t)$ , and it is formally defined by the point satisfying  $H_j(\vec{\xi}_j(t), t) = 0$ . For each fixed slab, the rastering pattern is such that it densely covers the entire  $xy$  imaging FOV, but without repeating over a position in that plane. This makes for what is essentially a 1-to-1 relationship in our discretized domains between time and FFP location.

### 3 Harmonic Portraits and PSFs for MH3D

#### 3.1 Harmonic Portrait Domain

For a single  $z$  slab location, the 2D rastering pattern within that plane is identical to all other  $z$  slab locations. Denoting this 2D plane FFP rastering pattern over time as  $(x_\xi(t), y_\xi(t))$ , then our 1-to-1 relationship is given by  $t \leftrightarrow (x_\xi(t), y_\xi(t))$ . We define a *portrait* slab image by gridding the time domain signal back to its  $xy$  FFP location. Specifically, this portrait slab is given by

$$d(x_\xi(t), y_\xi(t), z_j) = s(t; z_j). \quad (4)$$

Note that while the above portrait definition is well-defined, in order for such a portrait to be meaningful, we would first downsample  $s(t; z_j)$  to only sample once for each period of the transmit waveform, e.g. to sample at the points in which the FFP passes through  $z_j$ .

To obtain a harmonic portrait, we first apply a digital filter, also with downsampling, to isolate each integer harmonic obtaining  $s_k$  (see equation (24) in the appendix for details), which is the received signal filtered for the  $k$ th harmonic band. Then our harmonic portraits are given by

$$d_k(x_\xi(t), y_\xi(t), z_j) = s_k(t; z_j). \quad (5)$$

An example of a sequence of  $z$ -slab second and third harmonic portraits is shown in Figure 1 (a) and (b).

It is worth noting that converting the full time domain signals into the harmonic portrait domain is essentially a lossless data transformation since nearly all of the energy of the signals are concentrated at the harmonics. This observation is fundamental to the methodology, as it emphasizes that we should be able to achieve full imaging capabilities from the harmonic portrait domain.

### 3.2 Portrait PSFs and MH3D Model Overview

The model for our harmonic portrait image data is formally derived in the appendix, and the main ideas are outlined here. For each harmonic,  $k$ , the model for a portrait slab is given by<sup>2</sup>

$$d_k(x, y, z_j) = \vec{h}_k * \vec{\rho}_b(x, y, z_j), \quad (6)$$

where  $\vec{\rho}_b = \rho \cdot \vec{b}_1$ , and  $\vec{h}_k = (h_{kx}, h_{ky}, h_{kz})^\top$  are our harmonic portrait PSFs produced with sensitivity along the  $x$ ,  $y$ , and  $z$  axes at harmonic  $k$ .

These harmonic PSFs are the portraits that would be obtained by scanning a point source at the origin. Intuitively then, one may think of a more general harmonic portrait as containing a combination of point sources, which gives rise to the convolutional model above.

We can then write a matrix form of the complete data model utilizing harmonics 2 through  $K$  as

$$\begin{bmatrix} d_2 \\ d_3 \\ \vdots \\ d_K \end{bmatrix} = \begin{bmatrix} H_{2x} & H_{2y} & H_{2z} \\ H_{3x} & H_{3y} & H_{3z} \\ \vdots & \ddots & \vdots \\ H_{Kx} & H_{Ky} & H_{Kz} \end{bmatrix} \begin{bmatrix} B_x \\ B_y \\ B_z \end{bmatrix} \rho, \quad (7)$$

where

- $d_k$  are the discretized portraits for the  $k$ th harmonic.
- $H_{kx}$ ,  $H_{ky}$ , and  $H_{kz}$  are circulant matrices that represent the convolutional operations for each of the 3 components of  $\vec{h}_k$ .
- $B_x$ ,  $B_y$ , and  $B_z$  are diagonal matrices containing the receiver coil sensitivity weights in  $\vec{b}_1$ .

Note that all of these operators can be computed efficiently without excessive memory overhead using matrix-free operators (see for example [19, 20]).

Figure 2 shows a simulated example of an MH3D reconstruction of a simple phantom containing 3 objects, a square, triangle, and a circle, which are shown in the 3D volume rendering in the top right of the Figure. The square and triangle were modeled to be sitting in the  $z = -2$  cm plane, and the circle was modeled orthogonal to these two objects sitting in the  $y = 5$  cm plane. The received signal was simulated according to the scanning geometry described in Section 2, with a uniform receive sensitivity profile given by  $\vec{b}_1(\vec{x}) = (1, 1, 1)$  for all  $\vec{x}$ . While the complete algorithmic details of the MH3D model have yet to be provided, this example is provided as a proof of concept and to motivate the discussion that follows. The more generalized model-based reconstruction (see [19]) is also provided in the Figure as a baseline comparison. Observe that the two reconstructions are very similar in quality, resolution, and resulting minor image artifacts. The observed mild differences can likely be attributed to parameter selection, solver convergence, etc. This suggests that both models accurately utilize the complete set of information in the MPI received signal.

Notice that equation (7) contains 3 axis components, which completes a general form of the MH3D model. For many of our scanner applications we only model non-zero receive sensitivities along the  $z$  component of  $\vec{b}_1$ , as the other two components are negligible based on the receive coil design. With this simplification, we can reduce the model as

$$d_k(x, y, z_j) = (h_k * (b_z \cdot \rho))(x, y, z_j), \quad (8)$$

where it is implied that  $h_k$  now only contains the 3rd component from the  $\vec{h}_k$  vector. Then we can write the forward-matrix model needed to solve this associated inverse problem as

$$\begin{bmatrix} d_2 \\ d_3 \\ \vdots \\ d_K \end{bmatrix} = \begin{bmatrix} H_{2z} \\ H_{3z} \\ \vdots \\ H_{Kz} \end{bmatrix} B_z \rho. \quad (9)$$

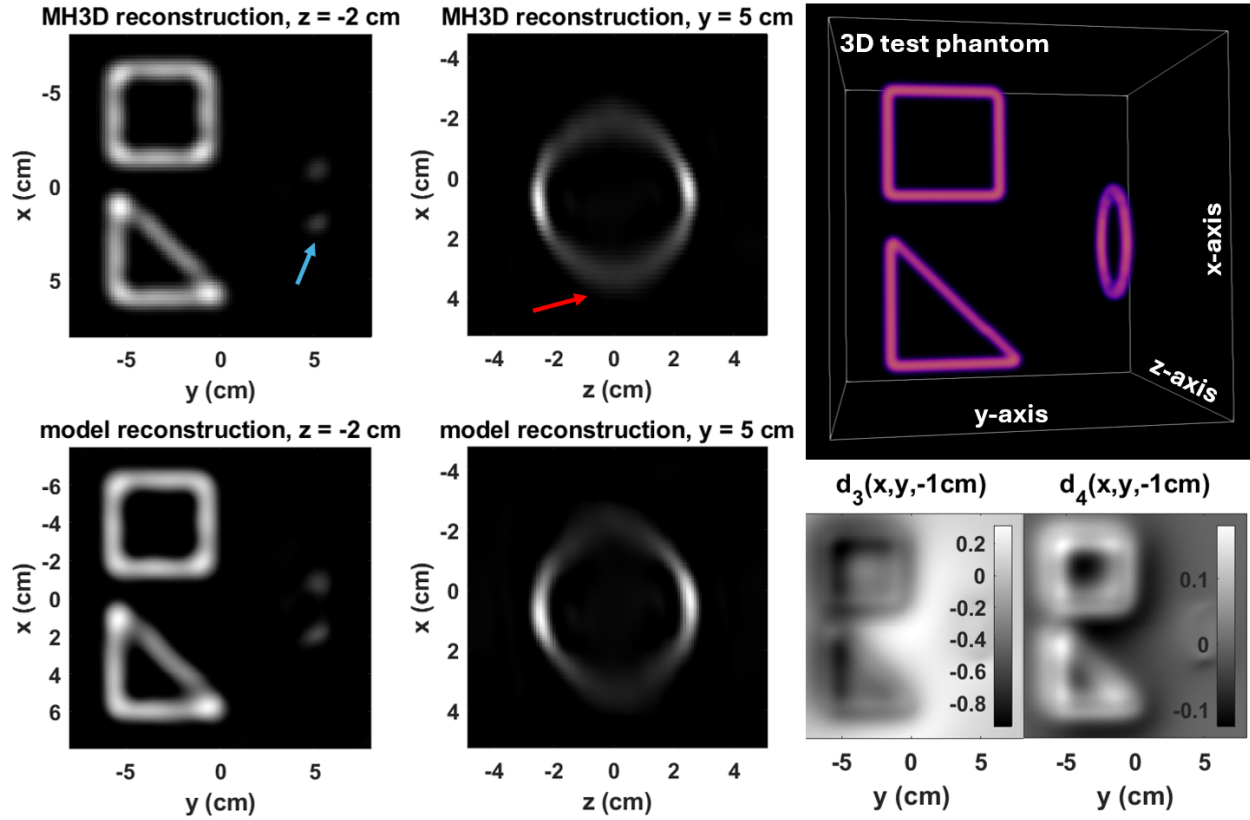


Figure 2: Comparison between the generalized model-based reconstruction [19] and the MH3D model presented in this work for a simulated 3D test phantom. The red arrow indicates some mild anisotropic blurring in the reconstruction inherently due to a  $z$ -axis only transmit. The blue arrow indicates where the circle passes through the  $z = -2$  cm plane and appears as two dots. The bottom right images show the 3rd and 4th harmonic portraits at  $z = -1$  cm. The top right image shows a 3D visualization of the simulated phantom. Note the similarity between the MH3D and model reconstruction images.

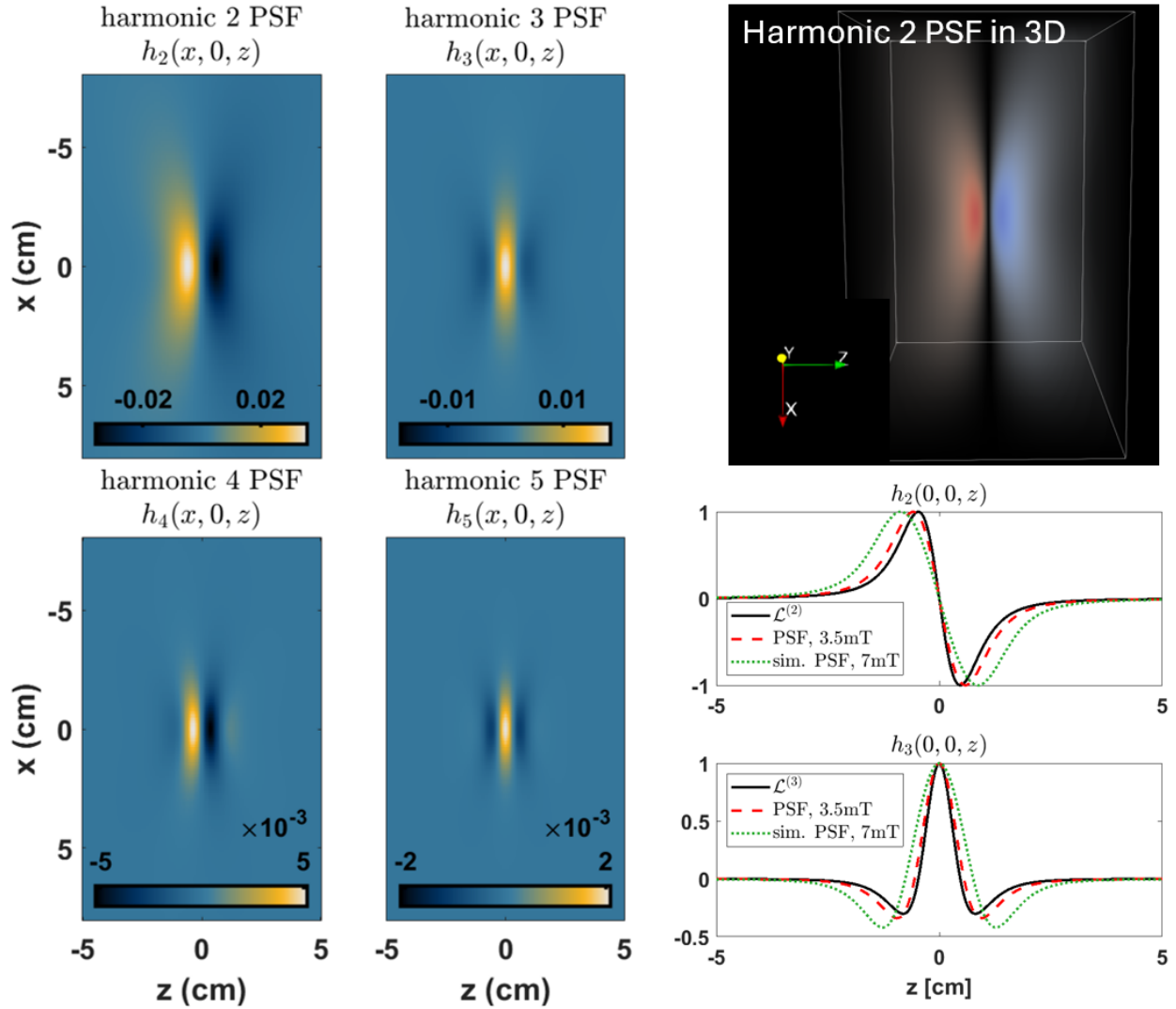


Figure 3: This figure illustrates of the harmonic PSFs shapes. Shown on the left are 2D images of the PSFs at  $y = 0$ , while noting that the PSFs are radially symmetric in the  $xy$  planes. The top right shows the 2nd harmonic PSF in a 3D rendering, where red and blue represent positive and negative values respectively. The bottom right plots show the PSFs at  $x = y = 0$  and compare 2 different PSFs arising from unique drive amplitudes with the PSF approximations given by the Langevin function's derivatives. The 1D plots are scaled by the maximum of each curve.

### 3.3 Harmonic PSF Approximations

The harmonic PSFs  $\vec{h}_k$  in equation (6) have been generated via simulations in practice. This is accomplished by simulating a spatially dense scan of a point source using the scanner parameters, such as transmit amplitude, gradient strength, and so on. This simulated data is then separated into its harmonic bands and gridded into the harmonic portrait domain. On one hand, it is possible to treat these simulated PSFs as a black box and simply use them for the deconvolution model. However, insight into their analytical form has proven useful in the development of this work, including additional modeling parameters, number of harmonics needed, validity of the methodology, and development of alternative methods (see sections 4.2 and Appendix D). Visualizations of the harmonic PSFs are shown in Figure 3.

We provide the general concept behind the harmonic PSFs in a 1D setting, while the full details are provided in the appendix. Suppose we have gridded the harmonics of a received signal and arrived at equation (8) with a uniform sensitivity now written as

$$d_k(x) = h_k * \rho(x). \tag{10}$$

Then our claim (see appendix) is that the 1D harmonic PSF  $h_k$  is approximated by

$$h_k(x) \approx c_k \mathcal{L}^{(k)}(\beta x), \tag{11}$$

where  $\mathcal{L}$  is the Langevin function and  $c_k$  are unique coefficient constants. In the 3D case with a  $z$ -axis drive and  $z$ -axis receive sensitivity, the  $k$ th harmonic PSF approximation generalizes as  $\frac{d^k}{dz^k} h_{33}(x, y, z)$ , where  $h_{33}$  is the last element of the MPI PSF tensor matrix [5]. The only caveat to this claim is that it is only particularly accurate for sufficiently small transmit amplitudes, e.g. those less than 10 mT (see Figure 3).

Formal details of this claim are provided in the appendix but only for a complex transmit waveform. The details for a real valued transmit waveform, which is the realistic case, are far more involved and go beyond the scope of this text. Therefore these details are reserved for future work.

## 4 Additional Modeling Considerations

### 4.1 Downsampling methods for Accurate Modeling

In an ideal setting, the portrait data  $d_k(x, y, z)$  would be sufficiently sampled in the discretized  $(x, y, z)$  space to approximate the true portrait in the continuous space. However, in our system and many others, the  $z$  axis is encoded via stepped mechanical translation, and due to the desire to limit scan acquisition times, the number of scanned  $z$ -locations is typically kept relatively low. In our case, the default distance between neighboring  $z$ -locations used is  $\Delta z = 5$  mm. At this distance the discretization of the continuous convolutional model along the  $z$ -axis can result in an undersampled model. The right images of Figure 4 demonstrates this by showing the PSF approximations when sampled at 1 mm and then at 5 mm. It can clearly be seen here that using the 5 mm mesh would notably undersample the PSF.

To overcome this issue, also demonstrated in Figure 4, we retain a high resolution model for the all of the forward operations, while simply applying a downsampling operation to the measured  $z$  locations as the final component of our model. In this way we are able to accurately approximate the continuous model at high resolution, while only downsampling to the actual scanned locations at the final stage. We have empirically found  $\Delta z \approx 1$  mm to be sufficient to accurately approximate the continuous model. Extending the matrix model given in (7) to this downsampling method arrives at

$$\underbrace{\begin{bmatrix} d_2 \\ d_3 \\ \vdots \\ d_K \end{bmatrix}}_{:=\mathbf{d}} = \underbrace{\begin{bmatrix} P & 0 & \dots & 0 \\ 0 & P & \dots & 0 \\ \vdots & & \ddots & 0 \\ 0 & 0 & \dots & P \end{bmatrix}}_{:=\mathbf{P}} \underbrace{\begin{bmatrix} H_{2x} & H_{2y} & H_{2z} \\ H_{3x} & H_{3y} & H_{3z} \\ \vdots & \ddots & \vdots \\ H_{Kx} & H_{Ky} & H_{Kz} \end{bmatrix}}_{:=\mathbf{H}} \underbrace{\begin{bmatrix} B_x \\ B_y \\ B_z \end{bmatrix}}_{\mathbf{B}} \rho, \tag{12}$$

$\mathbf{A} := \mathbf{P}\mathbf{H}\mathbf{B}$

<sup>2</sup>The vector valued convolution-dot product used here is defined as  $\vec{f} * \vec{g}(x) = \sum_{i=1}^N f_i * g_i(x)$ .



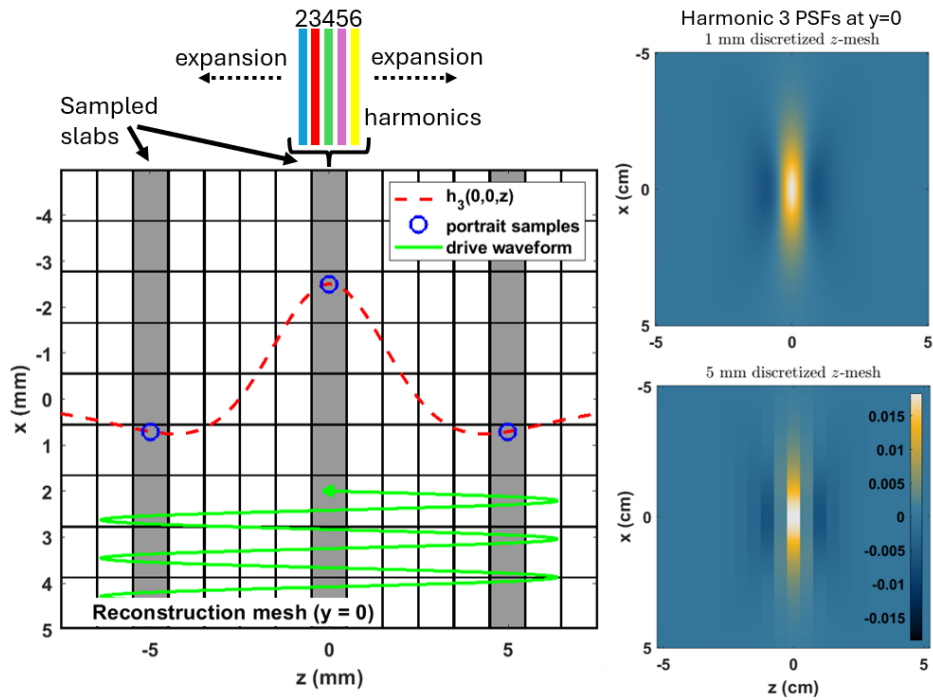


Figure 4: Imaging reconstruction mesh (left) showing the sampled portrait slab locations shaded in gray. The forward model uses the full high resolution mesh, while only downsampling to the portrait slabs as the final operation. The 3rd harmonic PSF at  $x = y = 0$  is overlaid onto the mesh to demonstrate how discretizing the full forward model at only the portrait slab locations would undersample the PSFs resulting in an inaccurate model. This is also demonstrated in the right images showing the PSFs at 1mm resolution and 5mm resolution in  $z$ . However, with multiple harmonics, the model can expand the information outward to positions between the measured slabs.

where  $P$  downsamples the result output from the first two high-resolution operators to only those  $z$  locations acquired in the scan. The full operator,  $\mathbf{P}$ , is written as a banded diagonal matrix, since this operation is applied for each harmonic. In matrix form,  $P$  is called a *row-selector* matrix, which contains only some rows of the identity matrix, i.e. a downsampling operation.

Note that using this model for the reconstruction also recovers  $\rho$  at the higher-resolution as defined by the first two operations, which generally improves the visual image quality. If we were using only a single harmonic, this added resolution may only provide additional pixels but not actual added resolution. However, the additional harmonics provides feasibility that this resolution is actually attainable, which we have observed empirically in simulations and with experimental data. The actual attainable resolution is highly system and scan dependent and should therefore be assessed accordingly.

One argument is that we have compressed the information from the entire transmit trajectory (see Figure 4) onto these portrait slabs and the reconstruction inherently re-expands this information along the  $z$ -axis (see the top of Figure 4). According to (11), we think of the reconstruction as performing a regularized expansion using the coefficients from the object’s Taylor expansion and/or its Chebyshev basis expansion [13]. For example, looking at equations (10) and (11), we could theoretically expand along a sampled point  $x$  to a nearby point  $x + \delta$  using a Taylor series approximation as

$$\mathcal{L}'_{\beta} * \rho(x + \delta) \approx \sum_{k=1}^K c_k^{-1} d_k(x) \frac{\delta^k}{k!}, \quad (13)$$

where  $\mathcal{L}'_{\beta}(x) = \mathcal{L}'(\beta x)$ . Hence, inherently the MH3D model reconstruction will be able to use this information to fill in the absent slab locations<sup>3</sup>.

Alternatively, from a simple linear algebra arguments about matrix rank, we could argue that given the  $K - 1$  harmonic portraits, we could in theory add in and accurately recover an additional  $K - 2$  locations in  $z$  between those that are measured. More precisely, suppose our portraits are gridded onto an imaging mesh of  $N_x \times N_y \times N_z$ , where  $N_z$  is the number of scanned  $z$ -slabs. Then the total number of data points given in harmonics 2 through  $K$  is  $N_x \cdot N_y \cdot N_z \cdot (K - 1)$ , and therefore a square linear forward model would be attained by setting the imaging mesh resolution to  $N_x \times N_y \times N_z \cdot (K - 1)$ . Using this argument, with our default sampling pattern at  $\Delta z = 5\text{mm}$ , a desired reconstructed resolution of  $1\text{mm}$  could be attained by using harmonics 2 through 6.

#### 4.1.1 Boundary Image Padding

The downsampling method just described was implemented to achieve both an accurate discretized forward model and high resolution image reconstructions. A similar method is described here and used for the separate purpose of reducing wrap-around artifacts that can be caused by digital convolution using FFTs. Namely, the computational convolutional operations implemented in our forward model are FFT-based. Unfortunately, FFT-based convolutions inherently are periodic and wrap around the boundaries. This can cause significant artifacts and image warping if not addressed. To overcome this, we pad the imaging FOV along the boundaries with additional pixels. The forward model includes these pixels, but an additional cropping is again implemented at the last step, which removes the additional boundary pixels since they are not in the portrait data. The reconstructed values obtained at these additional boundary pixels cannot be considered true image data in this case and are only used for artifact reduction within the scanned FOV. Therefore, they are simply discarded after the reconstruction is complete. We do not write down this extended model, since essentially the same model written in (12) applies to this methodology.

An example of MH3D with and without the boundary padding method is shown in Figure 5. In this example, a 2D spiral phantom was simulated with our default scanner parameters at the  $z = 0$  plane, and the simulation was set up so that the spiral is close to the edges of the scanned FOV in  $x$  and  $y$ . Observe that the MH3D reconstruction without padding results in distorted and blurred objects near the edges and additionally contains an extra dot-like object in the center at  $(0,0,0)$ . On the other hand, the MH3D boundary padded recon exhibits no such distortions or blurring effects. The pixels outside of the FOV box, which is drawn on the middle image, are typically discarded after the reconstruction is completed.

<sup>3</sup>Note that the fundamental harmonic at  $k = 1$  in equation (13) will not be available, which is addressed in Section 4.2.

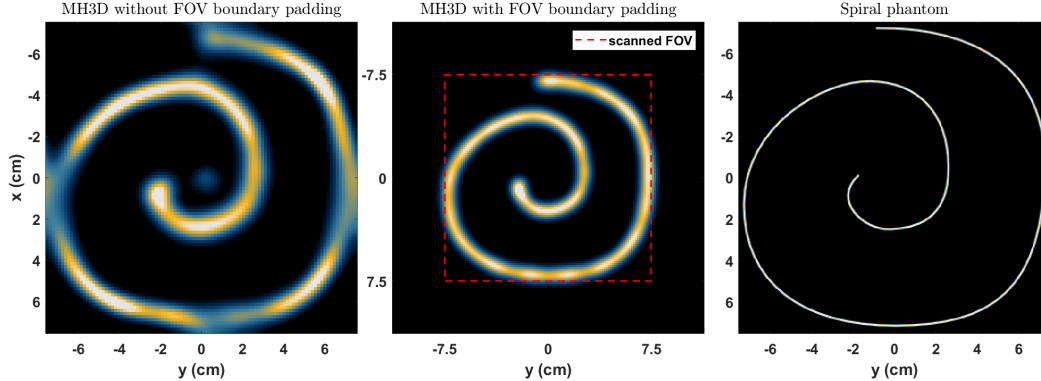


Figure 5: Shown are MH3D reconstructions with and without padding of a 2D spiral phantom with SPIONs near the edge of the scanned FOV. The padded reconstruction improves the image quality and eliminates the artifacts due to the SPIONs at the edge. The pixels outside of the red FOV box are typically discarded after the reconstruction.

## 4.2 Image Baseline and Artifact Reduction

Defining the data vector  $\mathbf{d}$  and the forward matrix model  $\mathbf{A}$  as indicated in (12), then our general inverse model for recovering  $\rho$  is given by

$$\rho^* = \arg \min_{\rho \geq 0} \|\mathbf{A}\rho - \mathbf{d}\|_2^2 + \lambda R(\rho), \quad (14)$$

where  $R$  is a regularization norm based on priors about the image  $\rho$ . The most basic form of the regularization that we have commonly used is a simple Tikhonov regularization given by

$$R(\rho) = \|T\rho\|_2^2, \quad (15)$$

where  $T$  is a finite difference operation, typically of 2nd order (see for example [20]). Intuitively, this regularization penalizes images with large derivatives encouraging *smooth* solutions. To numerically solve this model, we implemented a projected gradient descent with acceleration [1].

However, for MPI models we require an additional prior to account for the nature of the data. MPI harmonic data lacks the fundamental frequency component in the data due to drive interference and subsequent filtering at the fundamental frequency. In the Chebyshev basis analysis of the MPI signal [13], this is characterized by the missing fundamental basis coefficient, which effectively results in an unknown background constant. In terms of the MH3D methodology, there is a precise analogous description. The basic theory explains that the  $k$ th harmonic PSF is approximately proportional to the derivative of the  $k - 1$ st PSF as described in equation (11). Therefore, the 2nd harmonic PSF is approximately proportional to the 2nd derivative of the Langevin PSF (see Section 3.3). In a 1D hypothetical setting with a uniform sensitivity  $b_1 = 1$ , then our portrait would take the form

$$\begin{aligned} d_2(x) &= \mathcal{L}'' * \rho(x) \\ &= \frac{d}{dx} [\mathcal{L}' * \rho(x)], \end{aligned} \quad (16)$$

and so we could estimate the *native* image,  $\rho_N(x) = \mathcal{L}' * \rho(x)$ , by performing an anti-derivative:

$$\begin{aligned} \rho_N(x) &= \int d_2(x) dx = \int \frac{d}{dx} [\mathcal{L}' * \rho(x)] dx \\ &= \mathcal{L}' * \rho(x) + C. \end{aligned} \quad (17)$$

Hence with only the 2nd and higher harmonics, we are clearly still missing a background constant, which appears above in the MH3D domain as a result of integration.

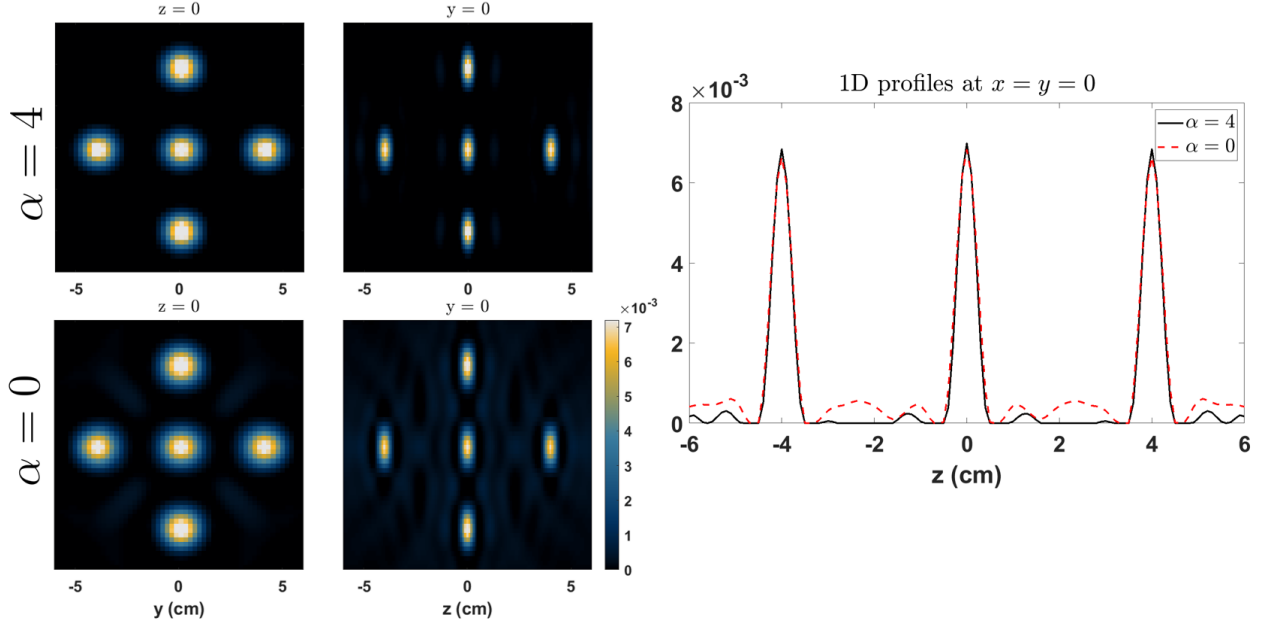


Figure 6: Simulated example demonstrating of the effect of the  $\alpha$  parameter and its ability to pin the background of the image to zero, significantly reducing unwanted ringing artifacts in the reconstructed image. The phantom image contains point source objects of uniform concentration, with one source  $(0, 0, 0)$  and the others located on the sphere of radius 4 cm centered around the origin.

In the classical X-space methods for MPI reconstruction, the unknown background is assumed to be zero, and therefore the image values are shifted to set the edges of the stitched images to zero to recover this lost information [5]. For the MH3D model, we compensate for this missing background by simply imposing a prior term in the regularization which encourages regions near the boundary of the field of view to be zero. We define this boundary set to be the “ $\alpha$ ” set and impose a penalty weight of  $\alpha$  on this region. To that end, our regularization used for MH3D is given by

$$R(\rho) = \|T\rho\|_2^2 + \alpha\|P_\alpha\rho\|_2^2, \quad (18)$$

where  $P_\alpha$  is a row selector matrix which selects the designated boundary pixels. This  $\alpha$  penalty has proven to be a fundamental component to the MH3D reconstruction by pushing the background level of the image to true zero, which in turn significantly reduces ringing artifacts in the final images.

A simulated example demonstrating the effect of  $\alpha$  is shown in Figure 6, where the phantom image used contains point source objects of uniform concentration, with one source  $(0, 0, 0)$  and the others located on the sphere of radius 4cm centered at the origin. Observe that there are significant background artifacts in the example where  $\alpha = 0$ , whereas the case  $\alpha = 4$  pushes this background near or close to zero and notably reduces artifacts.

### 4.3 Portrait Phase Calibration

Performing the harmonic filtering in  $k$ -space returns the harmonic signal data,  $s_k$ , as a complex valued vector, which results in complex valued portraits. However, thus far the descriptions of the MH3D portraits and PSFs have been real valued, e.g. the PSFs shown in Figure 3. Therefore we must understand and model for any phase information in the portraits to make MH3D robust.

There are a large number of system parameters that can change the phase of the data, which includes the analog receive chain filter, the digital harmonic filter design, phase shift of the transmit waveform, and even small time delays of the receive signal<sup>4</sup>. Figure 7 provides an example of how a small shift in the phase

<sup>4</sup>Recall that time domain shift results in a linear phase shift in  $k$ -space, which would then vary the phase from one harmonic to the next.

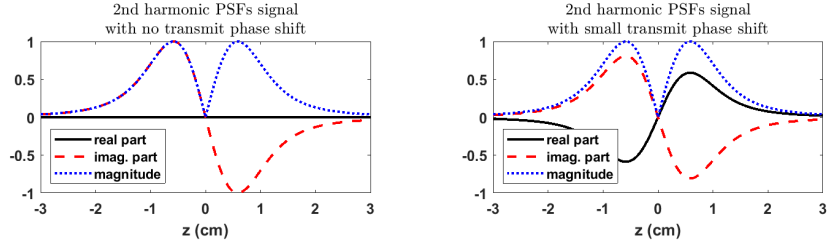


Figure 7: Example demonstrating how small changes in the signal can propagate into large changes in the phase of the harmonic portraits. On the left is a PSF simulated with an ideal sinusoidal transmit waveform, and on the right is the simulated PSF with a sinusoidal offset in phase by  $\pi/10$ , which results in a major change in the phase of the PSF.

of the transmit waveform results in a completely new phase in the resulting portrait PSF.

Due to this conglomeration of unique factors, tracking and compensating for each one is a non-practical method for adjusting for the phase in the harmonic data. Instead, we have developed a simpler, pragmatic method for correcting for the phase of the portraits directly in the portrait domain as a postprocessing step, which accounts for the net effect of all of the factors contributing to the observed phases.

The first key observation is that across a single relatively narrow band at a harmonic, the resulting phase observed in the portraits is a constant, which we have empirically confirmed with both simulations and real data. Therefore, we may write the non-ideal portrait containing a phase offset as

$$\tilde{d}_k = e^{i\theta_k} d_k, \quad (19)$$

where  $d_k$  is the ideal real valued portrait and  $\theta_k$  is the phase constant of the portrait. To estimate this phase value, we have calibrated it on high SNR samples, by measuring the phase observed in the portraits given by

$$\theta_k \approx \text{angle}(\tilde{d}_k(x, y, z)), \quad (20)$$

where we choose the values of  $(x, y, z)$  to be regions where the SNR is highest. However, there is one remaining ambiguity of  $\pi$  in this measured phase, since the portraits take both positive and negative values. To eliminate this ambiguity, we perform a simple unconstrained reconstruction with one of the phase values to determine if we need to flip the phase by the factor of  $\pi$ . The phase values only need to be calibrated once per receive coil, as we have a closed loop feedback in the hardware that ensures phase stability from scan to scan.

## 5 Results

### 5.1 Experimental Data

We provide two results using our MH3D reconstruction model on real experimental data containing VivoTrax (Magnetic Insight, Inc., Alameda CA.) with the 3D FFP scanner described in Section 2. The  $z$ -slab spacing for all data sets is  $\Delta z = 5$  mm, and the reconstructions utilized harmonic portraits 2-5.

The first example shown in Figure 8 contains an array of small vials at regularly spaced intervals, each containing 80 ug of VivoTrax. This phantom is useful for demonstrating the shift invariance of both the scanner and corresponding reconstruction. Shown in Figure 8(b) are cross-section images of the reconstruction from two different views. Observe that these images demonstrate consistency in the reconstructed SPION intensities across the entire imaging FOV, although with some variation in the shapes due to mild scanner inhomogeneities.

The second example is shown in Figure 9, which is a test phantom containing a 3D helical spiral taped around a head mannequin. This spiral also covers a most of the imaging FOV. The maximum intensity projections (MIPs) are shown in panel (a) of the Figure, where the maximum intensity is imaged across a single axis. A photo of the phantom used is shown in (b). Observe again that this reconstruction shows very

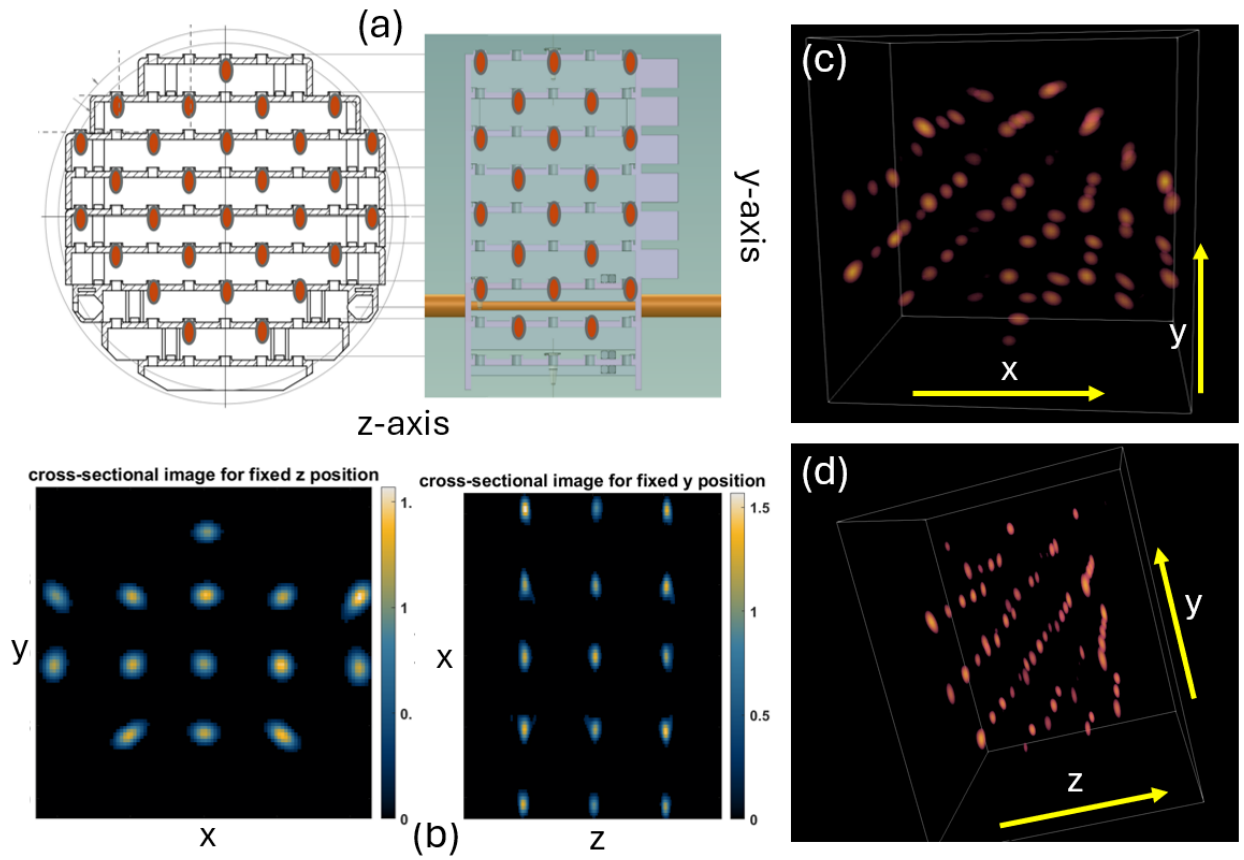


Figure 8: MH3D reconstructions of an experimental data set with a phantom containing an array of small vials of equal SPION volume (80 ug per vial) across the entire FOV, which is intended to test the linearity and shift invariance of the MPI scanner and reconstruction. (a) CAD model of the test phantom. (b) Cross-sectional images of the reconstruction. (c)-(d) 3D volume renderings of the reconstruction.

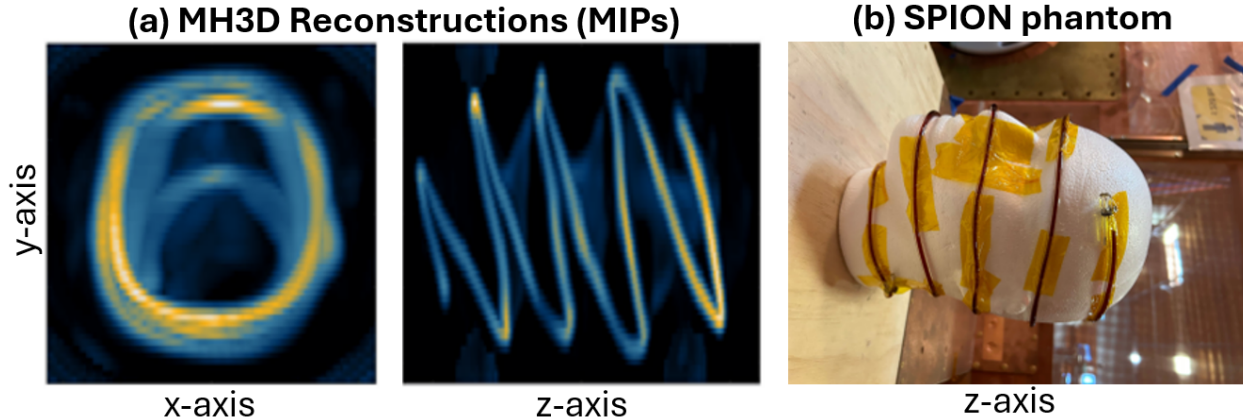


Figure 9: MH3D reconstructions of an experimental data set with a 3D helical spiral taped to a human head mannequin. (a) Maximum intensity projections (MIPs) of the MH3D reconstruction taken along the  $z$ -axis (left) and  $x$ -axis (right). (b) Photo of the test phantom.

few artifacts. This particular example highlights the potential for human head imaging applications in the future of MPI, which is in part facilitated by imaging analysis and reconstruction tools such as MH3D.

## 5.2 MH2D vs. Generalized Model

In this section we provide a simulated example of MH3D for a 2D FFL projection image, i.e. an example of MH2D. This example demonstrates how the MH3D methodology can generalize to alternative scanning geometries. In the simulations we mimicked the scanning patterns utilized by a production preclinical MPI scanner (Momentum, Magnetic Insight, Alameda, CA). The FFL focus fields for the Momentum scanner also raster in a zigzag Cartesian-like pattern, which is shown in the bottom right of Figure 10. The focus field shifts in this pattern in the  $xz$  plane, while the FFL direction is projected along the  $y$ -axis. This scan pattern is repeated twice, while the drive field alternates between the  $x$  and  $z$ -axis for both scans, with the collinear receive coil along the same axis.

The test image used for this simulation is shown in the top left of Figure 10 and is a spiral pattern of small point-like sources. The portraits may be formed on a Cartesian mesh, as shown in the bottom left of the figure. However, a more accurate portrait is used, which is formed by gridding the harmonic data precisely along the focus field pattern within the imaging mesh, as shown in the bottom middle image. The downsampling operator,  $\mathbf{P}$  from (12), is modified accordingly to downsample at the sampled pixel locations that can be seen in the image. Harmonics 2-5 were utilized for this example, and the resulting MH2D reconstruction is shown in the top middle panel of Figure 10. For comparison, the model-based reconstruction from [19] is shown in the top right and qualitatively returns a very similar result, with minor differences being attributed to parameter tuning and selection. This again demonstrates that both approaches fully utilize and model the data.

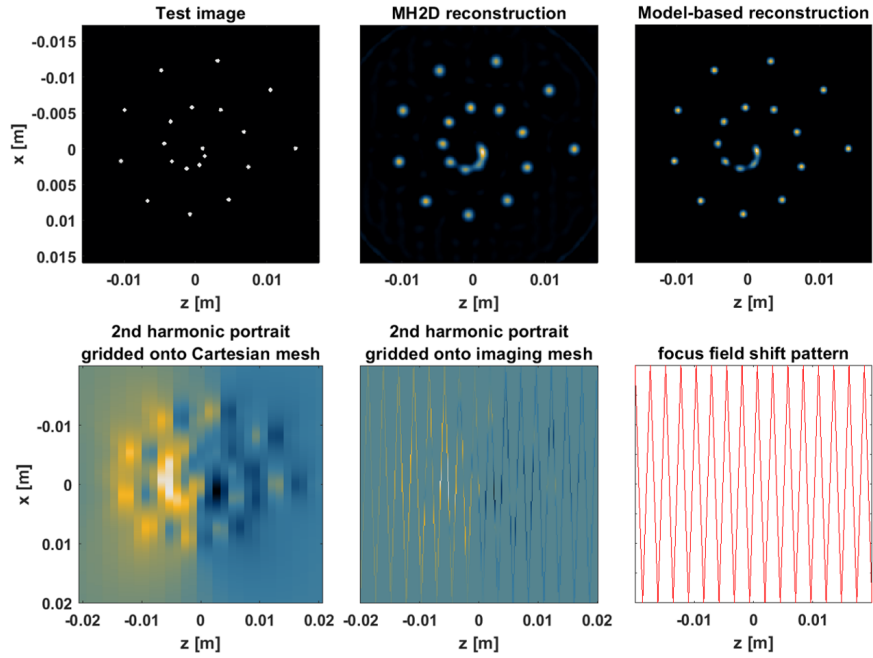


Figure 10: Shown is a simulated example demonstrating how the MH3D methodology extends to more scanning geometries, and in this case the example emulates a 2D projection scan image take by a Momentum (Magnetic Insight, Inc., Alameda, CA, USA) scanner. The MH2D reconstruction (top middle) obtains a very similar result to the generalized model-based reconstruction (top right) from [19]. The two images in the bottom left show two options for the portrait formation based on the FFL scanning pattern (shown in bottom right).



## 6 Summary

We have developed a new efficient model-based reconstruction for MPI to work in a common gridding domain, which have coined as the *portrait* domain. While this harmonic domain is not new to the field, we have developed a complete mathematical framework that is both computationally efficient and captures the full breadth of information in the MPI data. Our theoretical and empirical results show that the image reconstruction performance is comparable to a recently developed physics-based MPI model [19]. However, the new method provided here offers significantly improved data visualization, facilitating enhanced analysis and debugging, which have proven invaluable in our work. The drawback of this new method is that it requires additional re-engineering for new scanner configurations and pulse sequences, while the former model is easily amendable. Therefore, we believe that both methods will continue to have powerful utility within the field of MPI. Finally, the development of the new MH3D model has led to invaluable new theoretical insights into the nature of the MPI signal and the information attained at each of the higher harmonics, which we lay out in the appendix.

## A Analysis of the MH3D Harmonic PSFs

In this section we provide some theoretical analysis and insight into the harmonic PSFs arising from the MH3D model. These results allow us to understand and develop the image reconstruction models, while also providing new interesting theoretical insights into the harmonic analysis of MPI signals.

In all of the results that follow, we consider a 1D MPI model<sup>5</sup> with a static linear magnetic field given by  $Gx$  and SPION(s) with a conglomerate coefficient  $\beta$  (see Section 2 for details). We also reduce the Langevin function coefficient constants to a single coefficient defined by  $\gamma := \beta \cdot G$ , so that the SPION response to the applied magnetic field is

$$\mathcal{L}[\beta\|H\|] = \mathcal{L}[\gamma(\xi(t) - x)].$$

For simplicity in the derivations, we allow for our drive to take on a complex exponential waveform, which does not have an obvious real physical interpretation. However, it greatly simplifies the mathematical derivations, and similar but more tedious results are obtained with real trigonometric waveforms.

The following is the main result which provides an analytical decomposition of an MPI received signal into its harmonics. Among other things, this result shows us that the information at the  $k$ th harmonic effectively samples the  $k$ th derivative of the Langevin. The proof of this result is provided later in Appendix E to keep the flow of these results.

**Theorem 1.** *Suppose the FFP trajectory is given by a complex trigonometric waveform and a linear shift focus field given by*

$$\xi(t) = Ae^{i2\pi f_0 t} + t \cdot \Delta_t, \quad (21)$$

where  $|\gamma A| < \pi$  and  $\Delta_t$  is a linear shift rate constant, and let the SPION density be as single point source written as  $\rho(x) = \delta(x - x_0)$ . Then the noise-free and unfiltered MPI received signal is given by

$$s_0(t) = i2\pi m f_0 b_1(x_0) \sum_{k=1}^{\infty} \frac{(\gamma A)^k}{(k-1)!} \mathcal{L}^{(k)}[\gamma(t\Delta_t - x_0)] e^{i2\pi f_0 k t} + O(\Delta_t). \quad (22)$$

To extend this result further into the harmonic domain and to derive the portrait model, we apply harmonic filtering using the result from Theorem 1. The harmonic filtered signals,  $s_k(t)$ , are defined by window filtering for the band of frequencies in  $k$ -space around the chosen harmonic of  $s_0$ . There are many possible choices for a window filter around the frequency band (see Figure 11 for example), e.g. a Hann window or a top hat function. To complete the derivation we do not need to explicitly define this function, but we simply denote it by  $g(t)$ .

**Definition 1.** *Given a received signal  $s_0(t)$  and a window function  $g(t)$ , we define the  $k$ th harmonic filtered signal by*

$$s_k(t) := \int_{\mathbb{R}} \hat{s}_0(\omega + kf_0) \hat{g}(\omega) e^{i2\pi\omega t} d\omega, \quad (23)$$

---

<sup>5</sup>The results effectively apply in 2D and 3D, but would need to be modified so that the drive axis matches the axis of our 1D case used here. These derivations are provided in the supplementary material.

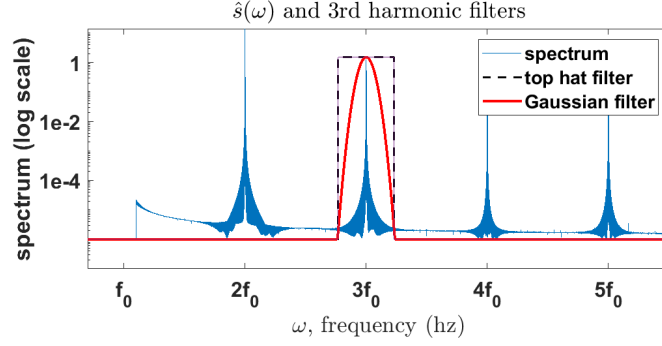


Figure 11: Example of a received signal's spectrum and possible window filters for the 3rd harmonic.

which may be reduced to

$$\begin{aligned}
s_k(t) &= \int_{\mathbb{R}} \hat{s}_0(\omega + kf_0) \hat{g}(\omega) e^{i2\pi\omega t} d\omega \\
&= \int_{\mathbb{R}} \int_{\mathbb{R}} s_0(\tau) e^{-i2\pi(\omega + kf_0)\tau} d\tau \hat{g}(\omega) e^{i2\pi\omega t} d\omega \\
&= \int_{\mathbb{R}} s_0(\tau) e^{-i2\pi kf_0\tau} \left[ \int_{\mathbb{R}} \hat{g}(\omega) e^{i2\pi\omega(t-\tau)} d\omega \right] d\tau \\
&= \int_{\mathbb{R}} s_0(\tau) e^{-i2\pi kf_0\tau} g(t-\tau) d\tau.
\end{aligned} \tag{24}$$

**Corollary 1.** Let  $s_k(t)$  be defined as in (24), and assume the same conditions as in Theorem 1. Assume a homogeneous receive sensitivity ( $b_1(x) = 1$ ) and  $x_0 = 0$ . Then the  $k$ th harmonic filtered signal for this point source is approximated by

$$s_{k,\delta}(t) \approx i2\pi m f_0 \frac{(\gamma A)^k}{(k-1)!} \int_{\mathbb{R}} \mathcal{L}^{(k)}(\gamma\tau \Delta_t) g(t-\tau) d\tau. \tag{25}$$

Therefore our harmonic PSF is given by gridding the harmonic time domain signal back to FFP focus field location, obtaining

$$\begin{aligned}
h_k(x) &= s_{k,\delta}(x\Delta_t^{-1}) \\
&\approx i2\pi m f_0 \frac{(\gamma A)^k}{\Delta_t(k-1)!} \int_{\mathbb{R}} \mathcal{L}^{(k)}(\gamma\tau) g((x-\tau)/\Delta_t) d\tau.
\end{aligned} \tag{26}$$

*Proof.* Combining (24) and (22) with a homogeneous receive coil obtains

$$\begin{aligned}
s_{k,\delta}(t) &\approx i2\pi m f_0 \sum_{j=1}^{\infty} \frac{(\gamma A)^j}{(j-1)!} \int_{\mathbb{R}} \mathcal{L}^{(j)}(\gamma\tau \Delta_t) e^{i2\pi f_0 \tau(j-k)} g(t-\tau) d\tau \\
&\approx i2\pi m f_0 \frac{(\gamma A)^k}{(k-1)!} \int_{\mathbb{R}} \mathcal{L}^{(k)}(\gamma\tau \Delta_t) g(t-\tau) d\tau.
\end{aligned} \tag{27}$$

In these approximations, we have dropped the small  $O(\Delta_t)$  term and used the fact that the integrals where  $j \neq k$  are negligible due to the rapid decay properties of the Fourier transform for smooth functions [8].

With the FFP focus point given by  $t\Delta_t$ , then the gridded harmonic portrait for this point source, which gives us the harmonic PSF, is given by

$$h_k(x) = s_{k,\delta}(x\Delta_t^{-1}), \tag{28}$$

which leads to (26).  $\square$

We note that Corollary 1 can be derived with equalities involving small additional terms related to the decay rates of the Fourier transform. However, the exact derivation significantly complicates the details without adding substantial value.

## A.1 Derivation of the Convolutional Portrait Model

If  $\rho(x)$  is a more general combination of point sources given as

$$\rho(x) = \sum_n \rho_n \delta(x - x_n), \quad (29)$$

then (22) generalizes to

$$s_0(t) = i2\pi m f_0 \sum_n b_1(x_n) \rho_n \sum_{k=1}^{\infty} \frac{(\gamma A)^k}{(k-1)!} \mathcal{L}^{(k)}[\gamma(t\Delta_t - x_n)] e^{i2\pi f_0 k t} + O(\Delta_t). \quad (30)$$

Using this expression and repeating similar steps to what was done in (27) and substituting  $\tau = \Delta_t^{-1}x_n + w$  obtains

$$\begin{aligned} s_k(t) &\approx i2\pi m f_0 \frac{(\gamma A)^k}{(k-1)!} \sum_n b_1(x_n) \rho_n \int_{\mathbb{R}} \mathcal{L}^{(k)}(\gamma(\tau\Delta_t - x_n)) g(t - \tau) d\tau \\ &= i2\pi m f_0 \frac{(\gamma A)^k}{(k-1)!} \sum_n b_1(x_n) \rho_n \int_{\mathbb{R}} \mathcal{L}^{(k)}(\gamma w \Delta_t) g(t - \Delta_t^{-1}x_n - w) dw \\ &= \sum_n b_1(x_n) \rho_n \underbrace{i2\pi m f_0 \frac{(\gamma A)^k}{(k-1)!} \int_{\mathbb{R}} \mathcal{L}^{(k)}(\gamma w \Delta_t) g(t - \Delta_t^{-1}x_n - w) dw}_{s_{k,\delta}(t - \Delta_t^{-1}x_n)} \\ &= \sum_n b_1(x_n) \rho_n s_{k,\delta}(t - \Delta_t^{-1}x_n). \end{aligned} \quad (31)$$

Thus we have arrived at a relationship between the general harmonic filtered signal and the single point source harmonic filter signal resembling something similar to a convolution. To complete the portrait convolutional relationship, similar to above we again map  $s_k$  to the portrait domain by gridding time points onto their FFP focus field locations, which obtains

$$\begin{aligned} d_k(x) &= s_k(x\Delta_t^{-1}) \\ &= \sum_n b_1(x_n) \rho_n s_{k,\delta}((x - x_n)\Delta_t^{-1}) \\ &= \sum_n b_1(x_n) \rho_n h_k(x - x_n) \\ &= \rho_b * h_k(x). \end{aligned} \quad (32)$$

## B Connection between the Generalized Model and MH3D

Both MH3D and the generalized MPI reconstruction model introduced in [19] rely on the following form of the received signal

$$s_0(t) = m \iiint \rho(\vec{x}) \vec{b}_1^T(\vec{x}) \vec{h}(\vec{\xi}(t) - \vec{x}) \vec{\xi}(t) d\vec{x}, \quad (33)$$

from which the discretized linear matrix model is given by

$$\vec{s}_0 = V E H B \rho. \quad (34)$$

This discretized model encapsulates each of the components from the continuous integral formulation in (33). Namely,  $V$  accounts for the velocity component,  $E$  accounts for the FFP location,  $H$  accounts for  $\vec{h}$  as the magnetic convolutional component, and  $B$  accounts for the receive sensitivity.

The MH3D model applies a harmonic filter and then a gridding operation to the received signal  $s_0$ . We write these two operations as  $C_k$  and  $\mathcal{I}_{t,x}$  respectively, which is expressed as

$$\begin{aligned}
d_k &= \mathcal{I}_{t,x} C_k s_0 \\
&= \mathcal{I}_{t,x} C_k V E H B \rho
\end{aligned} \tag{35}$$

On the other hand, according to (7) we have

$$d_k = \mathbf{H}_k B \rho, \tag{36}$$

where  $\mathbf{H}_k = [H_{kx}, H_{ky}, H_{kz}]$ , and  $B = [B_x, B_y, B_z]^\top$  is the same matrix as in (33). Based on this line of reasoning, we deduce that

$$\mathcal{I}_{t,x} C_k V E H = \mathbf{H}_k. \tag{37}$$

While this is not a formal proof of equivalence between the models, this paper demonstrates a striking resemblance between the two as shown in the images output in Figures 2 and 10.

## C The Information at Each Harmonic

Here, we provide intuition and details of the information contained in each harmonic portrait. Observe from equations (10) and (11) that we are approximately sampling the SPION density convolved with derivatives of the Langevin function. If we were able to measure the first harmonic with infinite SNR, leaving us with  $\rho$  convolved with the first derivative of the Langevin function, then this would have sufficient information to restore  $\rho \geq 0$ , since  $\mathcal{L}'$  is a positive function which decays rapidly akin to a Gaussian PSF. In this case, we would only need to deconvolve this result. However, since we only observe  $\rho$  convolved with 2nd and higher derivatives of the Langevin, certain objects in  $\rho$  would fall into a null space, and thus be un-recoverable. For example, since

$$0 = \int \mathcal{L}''(x) dx, \tag{38}$$

then it is easy to see that any constant background in  $\rho$  would be completely eliminated in the higher harmonics. Likewise, any polynomial of degree  $k$  in  $\rho$  is eliminated by convolving  $\rho$  with  $\mathcal{L}^{(k+2)}$ . To that end, we can intuit that the lower harmonics provide the most important information to restore the fundamental components of  $\rho$ , while the higher harmonics contain more functions in the null space. On the other hand, the higher harmonic PSFs are sharper and improve the resolution in the realistic case where the SNR is limited (see Section 4.1 for details).

To proceed with this argument more formally, we first set  $\gamma = 1$  in the argument of the Langevin function to simplify the discussion, without any loss of generality. Let's consider  $\rho$  to be a nonnegative and continuous infinitely differentiable function on some bounded interval  $[a, b]$  and denote this space of functions by

$$\mathcal{S} := \{\rho(x) \mid \rho(x) \geq 0 \text{ and } \rho \in C^\infty[a, b]\}. \tag{39}$$

Next, let's define the set of functional operators acting on  $\mathcal{S}$  by

$$\mathbb{F}_k(\rho) := \mathcal{L}^{(k)} * \rho(x), \tag{40}$$

for  $k \geq 1$ , while noting that the range of  $\mathbb{F}_k$  is effectively the set of functions that can be seen in the  $k$ th harmonic portrait domain. Then it is easy to deduce that  $\text{null}(\mathbb{F}_1) = \emptyset$ , while for  $k \geq 2$ , the null space of  $\mathbb{F}_k$  contains polynomials of degree strictly less than  $k - 1$ . So as  $k$  increases, the respective null space also increases. Hence with infinite SNR, then any functions that we are able to recover from the range of  $\mathbb{F}_k$  we are also able to recover from  $\mathbb{F}_{k-1}$ .

In summary, the lower harmonics provide the fundamental information needed to recover the image structure. The first harmonic is the only harmonic that retains the background constant of the image, so within MPI we must make assumptions about the image background, which has typically assumed that the regions near the boundaries are zero (see Section 4.2 for details). The second harmonic retains all other image information, and more fundamental image information is lost as the harmonic number increases. However, the higher harmonics provide higher SNR information about the function's derivatives, which improves the resolution of the images when dealing with pragmatic MPI sampling patterns, which is discussed in Section 4.1.

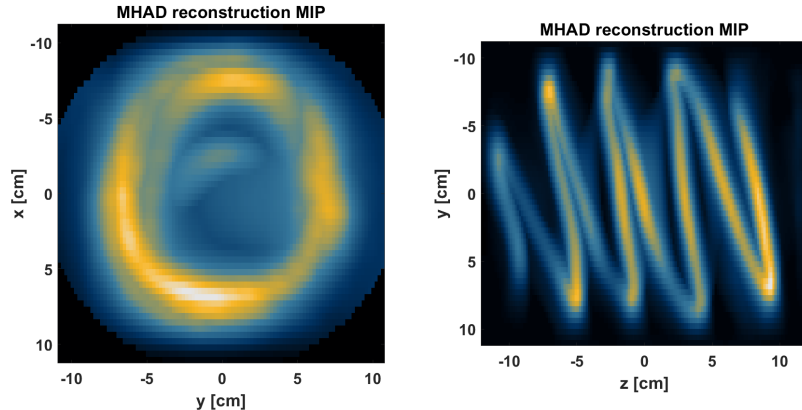


Figure 12: An example of a MHAD reconstruction using the same experimental dataset from the example shown in Figure 9.

## D MHAD: A Native Image Reconstruction based on Portrait Data

This section describes a simple native image reconstruction based on an anti-differentiation method from harmonic portraits, which we call multi-harmonic anti-differentiation (MHAD). The images returned from this method are approximately equivalent to those obtained from the X-space stitching method, while in practice particular nuances will be observed from each approach. However, for MHAD to work in practice, the portraits need to be sampled sufficiently dense for the discretized approximations used below to be accurate.

We continue our discussion in a 1D setting, but the same arguments apply in 3D (see supplementary material) where we only need to perform the derived methods along the transmit axis. Equation (17) shows how we may evaluate an anti-derivative with the 2nd harmonic portrait in the to estimate the native image, where the native image is defined by

$$\rho_N(x) = h * \rho(x) = \mathcal{L}' * \rho(x)$$

as described in [4]. To make this useful in a practical setting, we need a discrete method for anti-differentiation. Let us write a discretized model for the derivative at the 2nd harmonic by

$$d_2[j] = \rho_N[j + 1] - \rho_N[j - 1] + \epsilon[j], \quad (41)$$

where  $j$  is the pixel index and  $\epsilon$  is a noise term. For computational purposes, we will make this derivative circulant so that we can write it as a convolution given by

$$d_2 = f * \rho_N + \epsilon, \quad (42)$$

where  $f^T = [0, -1, 0, \dots, 0, 1]$ . Then we may write a 2nd harmonic only regularized MHAD model as

$$\begin{aligned} \rho_N^* &= \arg \min_{\rho} \|f * \rho - d_2\|_2^2 + \lambda \|\rho\|_2^2 \\ &= \mathcal{F}^{-1} \left[ \frac{\overline{\hat{f}}}{|\hat{f}|^2 + \lambda} \cdot \hat{d}_2 \right], \end{aligned} \quad (43)$$

where  $\mathcal{F}$  is the discrete Fourier transform and the hats denote the Fourier transforms of the vectors (see [20] for details and examples of more interesting regularizers).

To arrive at the full multi-harmonic version, we write

$$f^k = \underbrace{f * f * \dots * f}_{k \text{ times}},$$

and introduce relevant scaling factors for each portrait given by  $c_k = \frac{(\gamma A)^k}{(k-1)!}$  (see Appendix A for details). Then our more general portrait model at the  $k$ th harmonic is given as

$$d_k = c_k \cdot f^{k-1} * \rho_N + \epsilon_k.$$

Then the complete MHAD solution is given by

$$\begin{aligned} \rho_N^* &= \arg \min_{\rho} \sum_{k=2}^K \|f^{k-1} * \rho - c_k^{-1} d_k\|_2^2 + \lambda \|\rho\|_2^2 \\ &= \mathcal{F}^{-1} \left[ \frac{\sum_k c_k^{-1} \widehat{f^{k-1}} \cdot d_k}{\sum_k |\widehat{f^{k-1}}|^2 + \lambda} \right]. \end{aligned} \quad (44)$$

Note that convenience of the analytical MHAD solutions written in (43) and (44) is that the computational method for solving them only requires a few FFTs and are therefore extremely cheap computational solutions.

## E Proof of Theorem 1

To prove Theorem 1 we first establish a few basic propositions that will be needed. The first is a simple and well-known result [4].

**Proposition 1.** *Consider a 1D MPI signal model with an FFP at time  $t$  given by  $\xi(t)$  and a total magnetic field given by  $H(x, t) = G(\xi(t) - x)$ . Then the unfiltered received signal for an arbitrary SPION density  $\rho(x)$  is given by*

$$s_0(t) = m\gamma\xi'(t) \cdot \rho_b * h(\xi(t)), \quad (45)$$

where  $h(x) = \mathcal{L}'(\gamma x)$  and  $\rho_b(x) = \rho(x) \cdot b_1(x)$ .

*Proof.* Recall the unfiltered received signal in 1D MPI is given by

$$\begin{aligned} s_0(t) &= m \frac{d}{dt} \int b_1(x) \rho(x) \mathcal{L} [\gamma G^{-1} H(x, t)] dx \\ &= m \int \rho_b(x) \frac{d}{dt} \mathcal{L} [\gamma(\xi(t) - x)] dx \\ &= m\gamma\xi'(t) \int \rho_b(x) \mathcal{L}' [\gamma(\xi(t) - x)] dx \\ &= m\gamma\xi'(t) \cdot \rho_b * h(\xi(t)). \end{aligned} \quad (46)$$

□

The following is a well-known theorem that can be found in any standard text in complex analysis.

**Theorem 2.** *Suppose  $f(z)$  is an analytic function near  $z = a$  in the complex plane. Then  $f(z)$  has a power series expansion of the form*

$$f(z) = \sum_{k=0}^{\infty} f^{(k)}(a) \frac{(z-a)^k}{k!},$$

and the radius of convergence of this series is the largest value of  $R$  such that  $f(z)$  is analytic on the set  $\{|z-a| < R\}$ .

**Proposition 2.** Let  $h(x) = \mathcal{L}'(\gamma x)$ , where  $\gamma > 0$  and  $\mathcal{L}$  is the Langevin function given by  $\mathcal{L}(x) = \coth(x) - 1/x$ . Then a particular Taylor expansion of  $h$  is given as

$$h(a+b) = \sum_{k=0}^{\infty} h^{(k)}(a) \frac{b^k}{k!}, \quad (47)$$

which converges for

$$|\gamma b| < \sqrt{\gamma^2 a^2 + \pi^2}.$$

Proof of proposition 2 does not require a detailed calculation, but rather a careful analysis of the Langevin function and the corresponding convergence of its Taylor series according to Theorem 2. In particular, the Langevin function (and its derivatives) have discontinuities in the complex plane at  $ik\pi$  with  $k$  being a nonzero integer. Then a typical Taylor series of the Langevin function written by

$$\mathcal{L}(x) = \sum_{k=0}^{\infty} \mathcal{L}^{(k)}(x) \frac{(x-a)^k}{k!},$$

converges for values  $|x| < \sqrt{a^2 + \pi^2}$ . Translating these concepts to our particular function  $h(x)$  completes the proposition.

Finally we have all of the ingredients necessary to prove the main result.

*Proof of Theorem 1.* Substituting the values for  $\xi(t)$  and  $\rho(x)$  into (45) obtains

$$\frac{s_0(t)}{m\xi'(t)b_1(x_0)} = \gamma \cdot h(Ae^{i2\pi f_0 t} + t\Delta_t - x_0). \quad (48)$$

Applying the expansion for  $h$  given in (47) to the above equation yields

$$\begin{aligned} \frac{s_0(t)}{m\xi'(t)b_1(x_0)} &= \gamma \cdot h(Ae^{i2\pi f_0 t} + t\Delta_t - x_0) \\ &= \gamma \sum_{k=0}^{\infty} h^{(k)}(t\Delta_t - x_0) \frac{A^k e^{i2\pi f_0 kt}}{k!} \\ &= \gamma \sum_{k=0}^{\infty} \frac{A^k}{k!} h^{(k)}(t\Delta_t - x_0) e^{i2\pi f_0 kt} \end{aligned} \quad (49)$$

Multiplying through by  $m\xi'(t)b_1(x_0)$  and performing rearrangements completes the proof.  $\square$

## F Multi-dimensional Derivation of the Portrait Model with a Single-Axis Transmit

Here we outline the details for the multi-dimensional derivation of the portrait model, which was more formally derived for the 1D case. Begin by recalling the unfiltered 3D MPI received signal is given by

$$\begin{aligned} s_0(t) &= m \iiint \rho(\vec{x}) \vec{b}_1^T(\vec{x}) \frac{G(\vec{\xi}(t) - \vec{x})}{\|G(\vec{\xi}(t) - \vec{x})\|} \mathcal{L}[\beta \|G(\vec{\xi}(t) - \vec{x})\|] d\vec{x} \\ &= m \vec{v}(t)^T \vec{h} * \vec{\rho}_b(\xi(t)) \\ &= m \sum_{i,j=1}^3 v_j(t) h_{ji} * (\rho b_i)(\xi(t)), \end{aligned} \quad (50)$$

where

- $\rho(\vec{x})$  is the SPION(s) we are imaging.

- $\vec{b}_1(\vec{x})$  is the receive coil sensitivity.
- $\vec{\xi}(t)$  is the FFP.
- $\beta$  is a conglomerate nanoparticle constant.
- $m$  is the magnetic moment.
- $G$  is the  $3 \times 3$  static magnetic gradient field matrix.
- $\vec{h}(\vec{x})$  is the  $3 \times 3$  PSF tensor function given by

$$\vec{h}(\mathbf{x}) := \left[ \mathcal{L}'(\|G\mathbf{x}\|/H_{sat}) \frac{G\mathbf{x}\mathbf{x}^T G^T}{\|G\mathbf{x}\|H_{sat}} + \mathcal{L}(\|G\mathbf{x}\|/H_{sat}) \left( I - \frac{G\mathbf{x}\mathbf{x}^T G^T}{\|G\mathbf{x}\|^2} \right) \right] \frac{G}{\|G\mathbf{x}\|}. \quad (51)$$

- $\vec{v}(t)$  is the FFP velocity.

We proceed with assuming a scan sequence and SPION density given as

$$\rho(\vec{x}) = \delta(\vec{x} - \vec{x}_0) \quad (52)$$

and

$$\vec{\xi}(t) = t \cdot \vec{\Delta} + A e^{i2\pi f_0 t} \cdot \vec{e}_3, \quad (53)$$

where  $\vec{\Delta}$  is some linear shift rate vector and  $\vec{e}_3 = (0, 0, 1)^T$ .

Inputting this into the last line of (50) and then using a Taylor expansion along the  $z$ -axis obtains

$$\begin{aligned} s_0(t) &\approx im2\pi f_0 \sum_{j=1}^3 A e^{i2\pi f_0 t} h_{3j}(t \cdot \vec{\Delta} + A e^{i2\pi f_0 t} \cdot \vec{e}_3 - \vec{x}_0) b_j(\vec{x}_0) \\ &= C \sum_{j=1}^3 b_j(\vec{x}_0) \sum_{k=0}^{\infty} \frac{h_{3j}^{(0,0,k)}(t \cdot \vec{\Delta} - \vec{x}_0)}{k!} A^{k+1} e^{i2\pi f_0(k+1)t}, \end{aligned} \quad (54)$$

where  $C = im2\pi f_0$ , and in the approximation we dropped the  $O(\|\vec{\Delta}\|)$  terms coming from the FFP velocity shift vector. In what follows we write  $h_{3j}^{(k)}$  to denote  $h_{3j}^{(0,0,k)}$  for notational convenience.

Filtering for the  $k$ th harmonic then leads to

$$\begin{aligned} s_k(t) &= \int s_0(\tau) e^{-i2\pi f_0 k \tau} g(t - \tau) d\tau \\ &\approx C \sum_{j=1}^3 b_j(\vec{x}_0) \frac{A^k}{(k-1)!} \int h_{3j}^{(k-1)}(\tau \vec{\Delta} - \vec{x}_0) g(t - \tau) d\tau. \end{aligned} \quad (55)$$

We may grid this signal back into the spatial domain to the FFP focus field point to form the portrait via  $t = (\vec{\Delta})^{-1} \vec{x}$ , where here it is implied that  $(\vec{\Delta})^{-1} \vec{x}$  will select any one of the shift direction which is nonzero for the inverse mapping. For example, if  $\Delta_y$  being the shift rate in  $y$  is nonzero, then we may define  $(\vec{\Delta})^{-1} \vec{x} := \Delta_y^{-1} y$ .

Making this substitution obtains

$$\begin{aligned} s_k(\vec{\Delta}^{-1} \vec{x}) &\approx C \sum_{j=1}^3 b_j(x_0) \frac{A^k}{(k-1)!} \int h_{3j}^{(k-1)}(\tau \vec{\Delta} - \vec{x}_0) g(\vec{\Delta}^{-1} \vec{x} - \tau) d\tau \\ &= C \sum_{j=1}^3 b_j(x_0) \underbrace{\frac{A^k}{(k-1)!} \int h_{3j}^{(k-1)}((\vec{x} - \vec{x}_0) - \Delta w) g(w) dw}_{=:(\vec{h}_k)_j(\vec{x} - \vec{x}_0)} \end{aligned} \quad (56)$$



For a generalized SPION source written as

$$\rho(\vec{x}) = \sum_n \rho_n \delta(\vec{x} - \vec{x}_n),$$

then (55) becomes

$$s_k(t) \approx C \sum_{j=1}^3 \sum_n \rho_n b_j(\vec{x}_n) \frac{A^k}{(k-1)!} \int h_{3j}^{(k-1)}(\tau \vec{\Delta} - \vec{x}_n) g(t - \tau) d\tau, \quad (57)$$

and the portrait is given by

$$\begin{aligned} d_k(\vec{x}) &= s_k(\vec{\Delta}^{-1} \vec{x}) \\ &\approx C \sum_{j=1}^3 \sum_n \rho_n b_j(\vec{x}_n) \frac{A^k}{(k-1)!} \int h_{3j}^{(k-1)}(\tau \vec{\Delta} - \vec{x}_n) g(\vec{\Delta}^{-1} \vec{x} - \tau) d\tau \\ &= C \sum_{j=1}^3 \sum_n \rho_n b_j(\vec{x}_n) \underbrace{\frac{A^k}{(k-1)!} \int h_{3j}^{(k-1)}((\vec{x} - \vec{x}_n) - \Delta w) g(w) dw}_{(\vec{h}_k)_j(\vec{x} - \vec{x}_n)} \\ &= C \sum_{j=1}^3 \sum_n \rho_n b_j(\vec{x}_n) (\vec{h}_k)_j(\vec{x} - \vec{x}_n) \\ &= C \cdot \vec{h}_k * \vec{\rho}_b(\vec{x}), \end{aligned} \quad (58)$$

where  $\vec{\rho}_b(\vec{x}) = \rho(\vec{x}) \cdot \vec{b}_1(\vec{x})$ .

## Acknowledgment

The authors would like to thank Albert Boggess for pointing out the important detail related convergence of the Taylor series in the complex plane.

## References

- [1] A. Beck and M. Teboulle. A fast iterative shrinkage-thresholding algorithm for linear inverse problems. *SIAM journal on imaging sciences*, 2(1):183–202, 2009.
- [2] J. Dulińska-Litewka, A. Łazarczyk, P. Hałubiec, O. Szafranski, K. Karnas, and A. Karewicz. Superparamagnetic iron oxide nanoparticles—current and prospective medical applications. *Materials*, 12(4):617, 2019.
- [3] B. Gleich and J. Weizenecker. Tomographic imaging using the nonlinear response of magnetic particles. *Nature*, 435(7046):1214–1217, 2005.
- [4] P. W. Goodwill and S. M. Conolly. The X-space formulation of the magnetic particle imaging process: 1-D signal, resolution, bandwidth, SNR, SAR, and magnetostimulation. *IEEE transactions on medical imaging*, 29(11):1851–1859, 2010.
- [5] P. W. Goodwill and S. M. Conolly. Multidimensional x-space magnetic particle imaging. *IEEE transactions on medical imaging*, 30(9):1581–1590, 2011.
- [6] P. W. Goodwill, J. J. Konkle, B. Zheng, E. U. Saritas, and S. M. Conolly. Projection x-space magnetic particle imaging. *IEEE transactions on medical imaging*, 31(5):1076–1085, 2012.

- [7] P. W. Goodwill, E. U. Saritas, L. R. Croft, T. N. Kim, K. M. Krishnan, D. V. Schaffer, and S. M. Conolly. X-space mpi: magnetic nanoparticles for safe medical imaging. *Advanced materials*, 24(28):3870–3877, 2012.
- [8] A. Iosevich and E. Lifyand. Decay of the fourier transform. *Analytic and geometric aspects. Birkhäuser/Springer, Basel*, 2014.
- [9] K.-J. Janssen, M. Schilling, F. Ludwig, and J. Zhong. Single harmonic-based narrowband magnetic particle imaging. *Measurement Science and Technology*, 33:095405, 2022.
- [10] T. Knopp and T. M. Buzug. *Magnetic particle imaging: an introduction to imaging principles and scanner instrumentation*. Springer Science & Business Media, 2012.
- [11] T. Knopp, A. Weber, et al. Local system matrix compression for efficient reconstruction in magnetic particle imaging. *Advances in Mathematical Physics*, 2015, 2015.
- [12] Y. Liu, H. Hui, S. Liu, G. Li, B. Zhang, J. Zhong, Y. An, and J. Tian. Weighted sum of harmonic signals for direct imaging in magnetic particle imaging. *Physics in Medicine & Biology*, 68(1):015018, 2022.
- [13] K. Lu. *Linearity, shift-invariance and resolution improvement for quantitative magnetic particle imaging*. University of California, Berkeley, 2015.
- [14] E. E. Mason, S. F. Cauley, E. Mattingly, M. Sliwiak, and L. L. Wald. Side lobe informed center extraction (slice): a projection-space forward model reconstruction for a 2d imaging system. *International Journal on Magnetic Particle Imaging IJMPI*, 8(1 Suppl 1), 2022.
- [15] E. E. Mason, E. Mattingly, K. Herb, M. Sliwiak, S. Franconi, C. Z. Cooley, P. J. Slantez, and L. L. Wald. Concept for using magnetic particle imaging for intraoperative margin analysis in breast-conserving surgery. *Scientific Reports*, 11:13456, 2021.
- [16] C. McDonough, J. Chrisekos, and A. Tonyushkin. Tomographic magnetic particle imaging with a single-sided field-free line scanner. *IEEE Trans Biomed Eng.*, pages 1–12, 2024.
- [17] K. Nomura, M. Washino, T. Matsuda, S. Seino, T. Nakagawa, T. Kiwa, and M. Kanemaru. Development of human head size magnetic particle imaging system. *International Journal on Magnetic Particle Imaging*, 10, 2024.
- [18] N. Panagiotopoulos, R. L. Duschka, M. Ahlborg, G. Bringout, C. Debbeler, M. Graeser, C. Kaethner, K. Lüdtke-Buzug, H. Medimagh, J. Stelzner, et al. Magnetic particle imaging: current developments and future directions. *International journal of nanomedicine*, pages 3097–3114, 2015.
- [19] T. Sanders, J. Konkle, O. C. Sehl, A. R. Mohtasebzadeh, J. M. Greve, and P. W. Goodwill. A physics-based computational forward model for efficient image reconstruction in magnetic particle imaging. *IEEE Transactions on Medical Imaging*, 2025.
- [20] T. Sanders, R. B. Platte, and R. D. Skeel. Effective new methods for automated parameter selection in regularized inverse problems. *Applied Numerical Mathematics*, 152:29–48, 2020.
- [21] E. U. Saritas, P. W. Goodwill, L. R. Croft, J. J. Konkle, K. Lu, B. Zheng, and S. M. Conolly. Magnetic particle imaging (mpi) for nmr and mri researchers. *Journal of Magnetic Resonance*, 229:116–126, 2013.
- [22] O. C. Sehl, J. J. Gevaert, K. P. Melo, N. N. Knier, and P. J. Foster. A perspective on cell tracking with magnetic particle imaging. *Tomography*, 6(4):315–324, 2020.
- [23] O. C. Sehl, A. R. Mohtasebzadeh, K. Guo, P. Kim, B. Fellows, M. Weyhmiller, P. J. Foster, P. W. Goodwill, and J. M. Greve. First demonstration of magnetic particle imaging for sentinel lymph node identification. *Cancer Research*, 84(6\_Supplement):4135–4135, 2024.

- [24] N. Talebloo, M. Gudi, N. Robertson, and P. Wang. Magnetic particle imaging: Current applications in biomedical research. *Journal of Magnetic Resonance Imaging*, 51(6):1659–1668, 2020.
- [25] J. Weizenecker, B. Gleich, J. Rahmer, H. Dahnke, and J. Borgert. Three-dimensional real-time in vivo magnetic particle imaging. *Physics in Medicine & Biology*, 54(5):L1, 2009.
- [26] L. Zhang, J. Li, J. Du, G. Fang, D. Zhang, Z. Tang, H. Guo, and X. He. Current reconstruction approaches of magnetic particle imaging: A review. *Journal of Magnetism and Magnetic Materials*, page 171894, 2024.
- [27] B. Zheng, T. Vazin, P. W. Goodwill, A. Conway, A. Verma, E. Ulku Saritas, D. Schaffer, and S. M. Conolly. Magnetic particle imaging tracks the long-term fate of in vivo neural cell implants with high image contrast. *Scientific reports*, 5(1):14055, 2015.